Magnetoelectric response of quantum structures driven by optical vector beams

Jonas Wätzel, C. M. Granados-Castro, and Jamal Berakdar
Institute for Physics, Martin-Luther-University Halle-Wittenberg, 06099 Halle, Germany

(Received 22 October 2018; revised manuscript received 14 January 2019; published 19 February 2019)

Key advances in the generation and shaping of spatially structured photonic fields in both the near and far fields render possible the control of the duration, the phase, and the polarization state of the field distributions. For instance, optical vortices having a structured phase are nowadays routinely generated and exploited for a range of applications. While the light-matter interaction with optical vortices have been well studied, the distinctive features of the interaction of quantum matter with vector beams, meaning fields with spatially inhomogeneous polarization states, have yet to be explored in full detail, which is done here. We analyze the response of atomic and low-dimensional quantum structures to irradiation with radially or azimuthally polarized cylindrical vector beams. Striking differences from vortex beams are found: Radially polarized vector beams drive radially breathing charge-density oscillations via electric-type quantum transitions. Azimuthally polarized vector beams do not affect the charge at all but trigger, via a magnetic vector potential, a dynamic Aharonov-Bohm effect, meaning a vector-potential-driven oscillating magnetic moment. In contrast to vortex beams, no unidirectional currents are generated. Atoms driven by a radially polarized vector beam exhibit angular-momentum-conserving quadrupole transitions tunable by a static magnetic field, while when excited with an azimuthally polarized beam, different final-state magnetic sublevels can be accessed.

DOI: 10.1103/PhysRevB.99.085425

I. INTRODUCTION

Spatiotemporally modulated electromagnetic (EM) fields in general, and laser fields in particular, have been the driving force for numerous discoveries in science such as in femtochemistry and attosecond physics, both of which rely on the controlled temporal shaping of laser fields [1,2]. Spatially structured EM fields, which are currently the focus of research, have also proved instrumental for a wide range of applications such as particle trapping [3], high-resolution lithography [4–7], quantum memories [8], optical communication [9,10], and classical entanglement [11] and as a magnetic nanoprobe for enhancing the near-field magnetic component [12].

Prominent examples of structured EM fields are orbital-angular-momentum- (OAM) carrying vortex beams and vector beams (VBs). OAM beams possess an inhomogeneous azimuthal phase distribution and a homogeneous polarization. For VBs the spatial distributions of both the phase and the polarization in the plane perpendicular to the propagation of the EM wave are inhomogeneous. The spatial structuring brings about several advantages. For instance, a radially polarized VB allows for a sharper focusing. It may also have a strong centered longitudinal field [5], offering a tool for investigating new aspects of light-matter interaction, as detailed below. On the other hand, an azimuthally polarized VB has a smaller spot size than a radially polarized VB [4] and interacts with quantum matter in fundamentally different manner, as shown here. Phase-modulated beams carrying OAM [13] serve further purposes. For instance, such beams were used to study an otherwise inaccessible angular momentum state of atoms [14] and to generate unidirectional steady-state charge currents in molecular matter or in nanostructures [15,16], pointing to qualitatively new routes in optomagnetism.

Theoretically, key quantities for understanding the fundamentals of the interaction of structured fields with matter are the associated EM vector $\boldsymbol{A}(\boldsymbol{r},t)$ and scalar $\Phi(\boldsymbol{r},t)$ potentials that couple, respectively to the sample's currents and charge densities. Homogeneous optical EM fields irradiating a quantum object (with a charge localization below the EM field wavelength) induce mainly electric-dipole transitions in the sample and, to a much smaller degree, magnetic-dipole transitions. At moderate intensities, the ratio of the magnetic dipole to the electric dipole absorption rate is proportional to the ratio of the magnetic to electric field strengths $|\boldsymbol{H}|^2/|\boldsymbol{E}|^2$ [17]. Therefore, tailored laser beams with engineered magnetic to electric field ratio may boost the magnetic transitions. For instance, this can be accomplished in the near field of an object with a small circular aperture [18]. For the nanometer apertures experimentally feasible so far, the magnetic transition enhancement is negligibly small, however [18]. In this context, cylindrical VBs with azimuthal or radial polarization offer an interesting alternative. For azimuthally polarized VBs the magnetic to electric field ratio is substantial: one can show that $|\boldsymbol{H}|/|\boldsymbol{E}| = 1/\eta_0$ on the beam axis where η_0 is the free-space impedance [17,19]. The VBs we will be dealing with can be experimentally realized by the coherent interference of two TEM_{01} laser modes which are orthogonally polarized [20]. Other techniques involve interferometry [21], holograms [22], liquid-crystal polarizers [23], spatial light modulators [24], and multielliptical core fibers [25]. Planar fabrication technologies in connection with flat optics devices could also produce cylindrical VBs [26–28]. A further approach relies on the conversion of circularly polarized light into radially or azimuthally VBs (in the far-infrared [29] and visible

ranges [30]) by space-variant gratings. A method involving an inhomogeneous half-wave plate metasurface to generate VBs was also demonstrated [31,32] where the efficiency was increased when employing suitable metamaterials [19].

VBs possess a pronounced longitudinal component that can be employed for Raman spectroscopy [33], material processing [34,35], and tweezers for metallic particles [36]. For OAM-carrying beams, the longitudinal component may serve for studying subband states in a quantum well [37] and hole states in quantum dots [38]. The various facets of the interactions of VBs with quantum matter will be addressed in this work. As a demonstration of the formal theory, we will study the nature of bound-bound and bound-continuum transitions caused by VBs when interacting with quantum systems such as nanostructures and atoms. As demonstrated here not only is the interaction of such fields fundamentally different from nonstructured fields, but also radial VBs interact with matter in a qualitatively different way than azimuthal VBs do, and the employment of both offers qualitatively new opportunities for accessing the magnetoelectric response of quantum matter at moderate intensities.

II. LIGHT-MATTER INTERACTION WITH CYLINDRICAL VECTOR BEAMS

A cylindrical vector beam may be composed from two counterrotating circularly polarized optical vortex beams. The most prominent feature of such a vortex EM beam is the azimuthal phase structure described by $\exp(im_{\mathrm{OAM}}\varphi)$, where φ is the azimuthal angle in the xy plane [39,40], transverse to the propagation direction (which sets the z direction; the radial distance we denote by ρ). The parameter m_{OAM} is the vortex topological charge that determines the amount of the carried OAM and can potentially be transferred to a sample [15,38,41]. The wave vector along z is $q_\parallel$. Optical vortices have a phase singularity at $\rho = 0$ and thus a vanishing intensity at this point. Generally, the transverse spatial distribution is characterized by the function $f_{m_{\mathrm{OAM}}}(\rho)$, which can be, for instance, Laguerre-Gaussian type [39] or Bessel type [42], with the main difference being the radial intensity localization. For nanoscale objects centered in the vicinity of the optical axis, the different radial distributions of diffraction-limited vortex beams have similar influence (due to the vast difference between electronic and optical wavelengths). The change in this behavior with increasing OAM can be inferred from the fact that $f_{m_{\mathrm{OAM}}}(\rho) \sim \rho^{|m_{\mathrm{OAM}}|}$ for $\rho \to 0$. As an example, we concentrate on Bessel beams which are an exact solution of the Helmholtz equation [42], meaning that our theoretical considerations are beyond the paraxial approximation. Bessel beams are nondiffracting beam solutions with the radial profiles being independent of the propagation direction z, and the associated electromagnetic vector potential is a solenoidal vector field: $\nabla \cdot \boldsymbol{A}(\boldsymbol{r},t) \equiv 0$. For the electromagnetic field components ($\boldsymbol{r} = \{\rho, \varphi, z\}$ and Re indicates the real part), such vector potential reads

$$\boldsymbol{A}(\boldsymbol{r},t) = \mathrm{Re}\left\{ e^{i(q_\parallel z-\omega t)}\left[\hat{e}_\sigma J_{m_{\mathrm{OAM}}}(q_\perp\rho)e^{im_{\mathrm{OAM}}\varphi} - i\sigma\hat{e}_z\frac{q_\perp}{q_\parallel}J_{m_{\mathrm{OAM}}+\sigma}(q_\perp\rho)e^{i(m_{\mathrm{OAM}}+\sigma)\varphi}\right]\right\}, \tag{1}$$

where A_0 is the vector potential amplitude and ω is the light frequency. The longitudinal and radial (transverse) wave vectors satisfy the relation $q_\parallel^2 + q_\perp^2 = (\omega/c)^2$. The functions $J_n(x)$ are Bessel functions of nth order, while the polarization state is characterized by $\hat{e}_\sigma = e^{i\sigma\varphi}(\hat{e}_\rho + i\sigma\hat{e}_\varphi)$, with $\sigma = \pm 1$. The ratio $q_\perp/q_\parallel =: \tan\alpha$. Consequently, the angle α characterizes the spatial extent of the intensity profile. A large transverse wave vector means a tighter focusing. Since Bessel beams also satisfy the Coulomb gauge, the electric field reads $\boldsymbol{E}(\boldsymbol{r},t) = -\partial_t\boldsymbol{A}(\boldsymbol{r},t)$, while the magnetic field is given by $\boldsymbol{B}(\boldsymbol{r},t) = \nabla \times \boldsymbol{A}(\boldsymbol{r},t)$.

An azimuthally polarized cylindrical VB (which we refer to as AVB) can be expressed as a linear combination of two optical vortices with $\{m_{\mathrm{OAM}} = +1, \sigma = -1\}$ and $\{m_{\mathrm{OAM}} = -1, \sigma = +1\}$, namely,

$$\boldsymbol{A}_{\mathrm{AVB}}(\boldsymbol{r},t) = A_0 J_1(q_\perp\rho)\sin(q_\parallel z - \omega t)\hat{e}_\varphi. \tag{2}$$

A radially polarized cylindrical VB (denoted by RVB) is expressible as the difference of the two optical vortices,

$$\boldsymbol{A}_{\mathrm{RVB}}(\boldsymbol{r},t) = A_0\left[-J_1(q_\perp\rho)\cos(q_\parallel z - \omega t)\hat{e}_\rho + \frac{q_\perp}{q_\parallel}J_0(q_\perp\rho)\sin(q_\parallel z - \omega t)\hat{e}_z\right]. \tag{3}$$

A hallmark of AVB and RVB is the vanishing of the azimuthal-plane component of the field at $\rho = 0$. Moreover, AVB and RVB possess a nonvanishing longitudinal component: beams with the azimuthal polarization have a magnetic component at the origin, while the longitudinal component of the RVB is electric. The explicit electric and magnetic fields for both vector beam classes can be found in Appendix A.

We find that for both VBs the minimal coupling to matter is still viable, leading to the general interaction operator $\hat{H}_{\mathrm{int}}$ with a collection of charge carriers with effective mass m_e^* and charge $-e$,

$$\hat{H}_{\mathrm{int,tot}} = \sum_i \hat{H}_{\mathrm{int,i}},$$
$$\hat{H}_{\mathrm{int,i}} = -\frac{e}{2m_e^*}[\hat{\boldsymbol{p}}_i\cdot\boldsymbol{A}(\boldsymbol{r}_i,t) + \boldsymbol{A}(\boldsymbol{r}_i,t)\cdot\hat{\boldsymbol{p}}_i] + e\Phi(\boldsymbol{r}_i,t), \tag{4}$$

where $\hat{\boldsymbol{p}}_i$ is the linear momentum operator of particle i at position $\boldsymbol{r}_i$ [for moderate intensities we may suppress the term $\boldsymbol{A}^2(\boldsymbol{r}_i,t)$]. It is instructive to exploit the gauge invariance of observables and go over to the potentials (for brevity index i is suppressed),

$$\boldsymbol{A}'(\boldsymbol{r},t) = -\boldsymbol{r}\times\int_0^1 d\lambda\,\lambda\boldsymbol{B}(\lambda\boldsymbol{r},t) \tag{5}$$

and

$$\Phi'(\boldsymbol{r},t) = -\boldsymbol{r}\cdot\int_0^1 d\lambda\,\boldsymbol{E}(\lambda\boldsymbol{r},t). \tag{6}$$

The choice is referred to as the Poincaré gauge or, generally, the multipole gauge [43–45]. Note that in this gauge $\boldsymbol{r}\cdot\boldsymbol{A}'(\boldsymbol{r},t) \equiv 0$, and $\boldsymbol{B}(\boldsymbol{r},t) = \nabla\times\boldsymbol{A}'(\boldsymbol{r},t)$, while $\boldsymbol{E}(\boldsymbol{r},t) = -\partial_t\boldsymbol{A}'(\boldsymbol{r},t) - \nabla\Phi'(\boldsymbol{r},t)$. With Eqs. (5) and (6), the light-matter interaction can be expressed as the sum of pure electric and magnetic contributions, $\hat{H}_{\mathrm{int}} = \hat{H}_{\mathrm{el}} + \hat{H}_{\mathrm{magn}}$. *Field-charge*

coupling is captured by

$$\hat{H}_{\rm el}(t) = e\Phi'(\boldsymbol{r},t) = e\,\boldsymbol{r}\cdot\boldsymbol{E}'(\boldsymbol{r},t) \tag{7}$$

and $\boldsymbol{E}'(\boldsymbol{r},t) = -\int_0^1 d\lambda \boldsymbol{E}(\lambda\boldsymbol{r},t)$. The *orbital-Zeeman* coupling describes the interaction of the orbital magnetic moment with the magnetic field of the pulse,

$$\hat{H}_{\rm magn}(t) = 2\boldsymbol{B}'(\boldsymbol{r},t)\cdot\hat{\boldsymbol{m}}_B, \tag{8}$$

with the field $\boldsymbol{B}'(\boldsymbol{r},t) = -\int_0^1 d\lambda\,\lambda\boldsymbol{B}(\lambda\boldsymbol{r},t)$ and the orbital magnetic moment operator $\hat{\boldsymbol{m}}_B = (e/2m_0)\boldsymbol{r}\times\hat{\boldsymbol{p}}$ (for more details, see Appendix B). For a homogeneous field $\boldsymbol{B}'(\boldsymbol{r},t) = -\frac{1}{2}\boldsymbol{B}(t)$ we obtain the well-known dipolar magnetic interaction $\hat{H}_{\rm magn}(t) = -\hat{\boldsymbol{m}}_B\cdot\boldsymbol{B}(t)$. Considering a spin-active system with a spin-dependent field-free Hamiltonian $\hat{H}_0$ such as (with $\hat{\boldsymbol{\sigma}}$ being a vector of Pauli matrices)

$$\hat{H}_0 = \frac{\hat{\boldsymbol{p}}^2}{2m_e^*} + \frac{\alpha_R}{\hbar}[\hat{\boldsymbol{\sigma}}\times\hat{\boldsymbol{p}}]_z + V(\mathbf{r}), \tag{9}$$

where $V(\mathbf{r})$ is a scalar potential and α_R is the (Rashba) spin-orbital interaction (SOI) strength, we find the following expression upon applying the external VBs:

$$\hat{H} = \hat{H}_0 + \hat{H}_{\rm int}(t) + \hat{H}_{\rm SOI}(t) + \hat{H}_z(t). \tag{10}$$

The *spin-orbital-field* interaction $\hat{H}_{\rm SOI}(t) = -\frac{e\alpha_R}{\hbar}[\hat{\boldsymbol{\sigma}}\times\boldsymbol{A}(\boldsymbol{r},t)]_z$ transforms in the Poincaré gauge to

$$\hat{H}_{\rm SOI}(t) = -\frac{e\alpha_R}{\hbar}[\hat{\boldsymbol{\sigma}}\times(\boldsymbol{r}\times\boldsymbol{B}'(\boldsymbol{r},t))]_z. \tag{11}$$

The *spin-field-Zeeman* coupling reads

$$\hat{H}_z(t) = -\tfrac{1}{2}\mu_B g_s\hat{\boldsymbol{\sigma}}\cdot\boldsymbol{B}(\boldsymbol{r},t), \tag{12}$$

where μ_B is the Bohr magneton and g_s is the anomalous gyromagnetic ratio. In the static limit we recover the usual Zeeman coupling lifting the spin degeneracy [46–50]. Note that the vector beams can be designed to vary the ratio between the magnetic and electric field components. The Rashba spin-orbital coupling is also tunable, for instance, by gating. Thus, it is possible to access separately the various types of excitations in a sample: pure charge excitations, orbital-magnetic moment excitations, spin-orbital-coupled excitations, and spin-magnetic moment excitations. Below, we will illustrate this statement for two systems, a mesoscopic ring with spin-orbital coupling and an atomic target.

III. SPIN-ACTIVE QUANTUM RING STRUCTURES

For numerical demonstrations we consider quantum ring structures that are widely encountered in nature or synthesized in the laboratory, for example, molecular macrocycles and rotaxane structures [51–53]. Here, we inspect an appropriately doped quantum ring etched in a semiconductor-based two-dimensional electron gas. The conduction band charge carriers are tightly confined in the direction normal to the ring plane by the potential $U(z)$. In the ring plane the radially symmetric potential $V(\rho)$ defines the ring. The independent charge carriers are free to move in the azimuthal direction $\hat{e}_\varphi$. The (spin-degenerate) single-particle states are represented by the wave functions $\Psi_{n,m,k}(\rho,\varphi,z) = \frac{1}{\sqrt{2\pi}}\rho^{-1/2}R_{nm}(\rho)e^{im\varphi}Z_k(z)$ with the normalization $\int d\rho\, R_{nm}(\rho)R_{n'm}(\rho) = \delta_{n,n'}$ and $\int dz\, Z_k(z)Z_{k'}(z) = \delta_{k,k'}$. The particle number and $U(z)$ are chosen such that only the lowest subband $k=0$ is occupied. This can be achieved in a semiconductor-based structure by an appropriate gating. Henceforth, we omit therefore the index $k=0$ for brevity and trace out the z dependence. Furthermore, we checked that the driving field amplitude and its frequency do not cause any transitions to subbands with $k\neq 0$.

The time-independent single-particle Hamiltonian including SOI (9) has been already discussed extensively in several works [46–50], albeit for homogeneous EM fields. Considering intraband transition in the lowest radial subband $n=0$, the angular-dependent spin-resolved single-particle wave functions are

$$\Psi_m^s = N_n e^{i(m+1/2)\varphi}\nu^s(\gamma,\varphi), \tag{13}$$

where s and m denote the spin and integer angular quantum numbers and N_n stands for the normalization. The spinors

$$\nu^s(\gamma,\varphi) = (a^s e^{-i\varphi/2}, b^s e^{i\varphi/2})^T \tag{14}$$

are defined in the local frame with

$$a^\uparrow = \cos(\gamma/2),\ b^\uparrow = \sin(\gamma/2) \tag{15}$$

and

$$a^\downarrow = -\sin(\gamma/2),\ b^\downarrow = \cos(\gamma/2). \tag{16}$$

The angle γ defines the direction of the spin relative to $\hat{e}_z$ with a value set by SOI strength: $\tan(\gamma) = -\omega_R/\omega_0$, where $\hbar\omega_R = 2\alpha_R/\rho_0$ and $\hbar\omega_0 = \hbar^2/(m_e^*\rho_0^2)$, is the inherent energy scale of a ring with a radius ρ_0. The local spin orientations are inferred from the relations

$$S_\uparrow(\boldsymbol{r}) = \frac{\hbar}{2}[\sin(\gamma)\cos(\varphi)\hat{e}_x + \sin(\gamma)\sin(\varphi)\hat{e}_y + \cos(\gamma)\hat{e}_z] \tag{17}$$

for the spin-up states, while the spin-down states are characterized by

$$S_\downarrow(\boldsymbol{r}) = \frac{\hbar}{2}[\sin(\pi-\gamma)\cos(\pi+\varphi)\hat{e}_x + \sin(\pi-\gamma)\sin(\pi+\varphi)\hat{e}_y + \cos(\pi-\gamma)\hat{e}_z]. \tag{18}$$

The associated eigenenergies are given by

$$E_m^s = \frac{\hbar\omega_0}{2}\left[(m-x_s)^2 - \frac{Q_R^2}{4}\right], \tag{19}$$

where $x_s = -(1-sw)/2$ and $w = \sqrt{1+Q_R^2} = 1/\cos(\gamma)$. Furthermore, $s=\pm1$ stand for up and down spin states. We emphasize that, hereafter, the terms up and down (labeled, respectively, $\uparrow$ and $\downarrow$) refer to directions in the local frame $\{\gamma,\varphi\}$ [see Eqs. (17) and (18)]. The two characteristic spin bands are separated from each other by w, which, in return, depends on the strength of the spin-orbit coupling α_R.

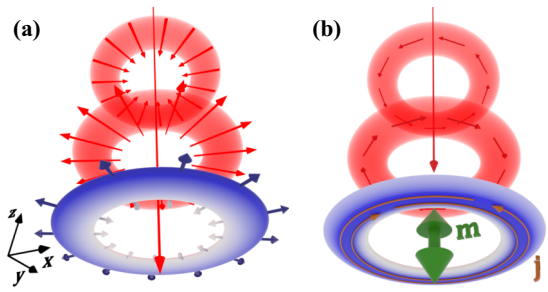

FIG. 1. Quantum ring (charge density is marked in blue) irradiated by a cylindrical vector beam (red rings at two different times). (a) The radially polarized vector beam initiates electric-type transitions leading to uniform radially breathing charge density (nondipolar collective charge excitations). (b) The azimuthally polarized vector beam drives homogeneously oscillating transient currents (orange arrows), giving rise to an oscillating magnetic dipole moment (green arrow). The frequency is set by the driving field. In both cases no unidirectional charge currents are generated.

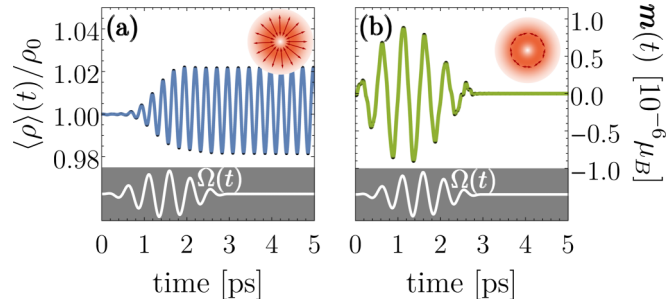

FIG. 2. Dynamics from full numerical quantum simulation: (a) time-dependent averaged value $\langle\rho\rangle(t)$ of a quantum ring driven by RVB with a six-optical-cycle duration, causing a radial dipole excitation. The oscillation frequency can be identified by $(E_{n=1} - E_{n=0})/\hbar$. (b) The time-dependent magnetic moment in the z direction of a quantum ring driven by AVB. The white curves represent the normalized electric field amplitude of the incident light pulses with an intensity $I \sim 10^4\,\mathrm{W/cm^2}$ in the area of the ring, and $\hbar\omega = 8$ meV.

A. Electric transitions induced by radially polarized vector beams

The interaction of RVB with quantum rings is illustrated schematically in Fig. 1(a). The coupling to the electric charge is dominant, causing photoinduced transitions, meaning that $\hat{H}^{\mathrm{RVB}}_{\mathrm{int}}(t) = \hat{H}^{\mathrm{RVB}}_{\mathrm{elec}}(t)$. Positioning the nanostructure in the plane $z = 0$, the interaction with the RVB-associated magnetic field (see fields in the Appendix A) reads $\hat{H}^{\mathrm{RVB}}_{\mathrm{magn}}(t) = -2i\mu_B B'(\boldsymbol{r}, t)(z\partial_\rho - \rho\partial_z)$. Obviously, this has no influence on the confined electrons in the xy plane as long as the photon energy $\hbar\omega$ is smaller than the level spacing of the subbands associated with the confinements in the z direction [characterized by $U(z)$]. We note that in the following treatment the symmetry axis of the quantum ring coincides with the optical axis of the vector beam. Hence, RVBs induce electric transitions between states with the amplitude

$$M^{\mathrm{RVB}}_{\mathrm{int}}(t) = \left\langle \Psi^{s'}_{m'} \middle| \hat{H}^{\mathrm{RVB}}_{\mathrm{el}}(t) \middle| \Psi^{s}_{m} \right\rangle = \frac{eA_0\omega}{q_\perp}[J_0(q_\perp\rho_0) - 1]\sin(\omega t)\delta_{m',m}\delta_{s',s}. \tag{20}$$

Notably, *no* direct spin-flip transitions are induced by RVBs; in contrast to OAM-carrying optical vortex, *no* orbital angular momentum is transferred to the charge carriers, leading to the selection rule $\Delta m = 0$. Thus, in a strictly one-dimensional (1D) quantum ring angular momentum and spin states are unaffected.

In a more realistic two-dimensional (2D) quantum ring $n \to n'$ radial subband transitions are possible, with an amplitude (time averaged and to first order in the driving fields) proportional to the radial integral (under conservation of the azimuthal quantum number):

$$\mathcal{R}^{\mathrm{RVB}}_{n',n} = \int_0^\infty d\rho\, R_{n'm}(\rho)[J_0(q_\perp\rho) - 1]R_{nm}(\rho), \tag{21}$$

which occurs in Eq. (20) instead of $[J_0(q_\perp\rho_0) - 1]$. Here, $R_{nm}(\rho)$ characterizes the radial wave function of the electronic state $|\Psi^s_{nm}\rangle$. It follows that the excitation by RVB conserves the cylindrical symmetry.

This *radial electric excitation* has a volume character. In contrast, spatially homogeneous laser fields drive only dipolar collective charge (plasmons) excitations. For radial vector beams, even the field frequency is still in the range of collective charge excitations; nondipolar (bulk-type) excitations are possible. This can be understood for the ring case as follows: The evaluated local dipole moment is the same in all radial directions $\hat{e}_\rho$ and oscillates with a frequency characterized by the energy difference between both levels n and n'. As a result, the *averaged* total dipole moment is zero:

$$\boldsymbol{d}(t) = \int d\boldsymbol{r}\, \rho_e(\boldsymbol{r}, t) \cdot \boldsymbol{r} = 0, \tag{22}$$

where $\rho_e(\boldsymbol{r}, t) = \sum_{n,m} |\Psi_{n,m}(\boldsymbol{r}, t)|^2$ is the (driven) time-dependent charge density.

For detailed and reliable insight, we performed full-numerical space-time-grid propagation of the three energetically lowest electron states in an irradiated 2D quantum ring including the external fields to all orders. Figure 2(a) displays the resulting charge dynamics induced by the depicted few-cycle external RVB pulse. The ring radius is $\rho_0 = 50$ nm, and the effective width $\Delta\rho = 30$ nm. The RVB temporal envelope function $\Omega(t) = \sin[\pi t/T_p]^2$, where $T_p = 2\pi n_p/\omega$ sets the pulse length in terms of the number of optical cycles n_p. We consider a short pulse with $n_p = 6$ cycles and a photon energy $\hbar\omega = 8$ meV. The small nanostructure is localized in the low-intensity beam center and away from the first field intensity maximum. We found strong multiphoton processes and the ponderomotive contribution due to $\boldsymbol{A}^2(\boldsymbol{r}, t)$ to be negligibly small for the light intensity on the ring, which was in the range of $\sim 10^4\,\mathrm{W/cm^2}$. As predicted by the analytical treatment, we found that all the propagated wave functions keep the symmetry in the azimuthal direction at all times. Field-induced effects are caused by transitions to the second radial subband, leading to charge "breathing" oscillations in the radial direction (we start from the initial states $n = 0$, $m = -1, 0, 1$). The time-dependent radial expectation value $\langle\rho\rangle(t)$ oscillates with a frequency related to $(E_{n=1,m} - E_{n=0,m})/\hbar$. When the pulse is off, the prodded charge dynamics goes on

due to coherences, meaning that every electron state oscillates between the lowest two radial levels.

B. Magnetic transitions induced by azimuthally polarized vector beams

The schematics of an AVB and its action on a quantum ring are shown in Fig. 1(b). It is straightforward to demonstrate that the associated electric contribution to the light-matter Hamiltonian $\hat{H}_{\rm int}(t)$ vanishes in the geometry depicted in Fig. 1(b): the electric field is perfectly azimuthally polarized, and therefore, $\boldsymbol{r}\cdot\boldsymbol{E}'(\boldsymbol{r},t)\equiv 0$. Thus, the AVB induces *no* electric (dipole) moment.

The light-matter interaction Hamiltonian reduces to $\hat{H}_{\rm int}(t)\equiv\hat{H}^{\rm AVB}_{\rm magn}(t)$. Note that the contribution to the magnetic interaction of the type $\hat{e}_z\cdot\hat{\boldsymbol{m}}_B=-i\mu_B\partial_\varphi$ does not affect the magnetic quantum number; that is, the selection rule $\Delta m=0$ is obtained. Generally, the interaction matrix elements have the explicit form

$$\begin{aligned}M^{\rm AVB}_{\rm int}(t)&=\left\langle\Psi^{s'}_{m'}\middle|\hat{H}^{\rm AVB}_{\rm magn}(t)\middle|\Psi^{s}_{m}\right\rangle\\&=-\mu_B\frac{A_0}{\rho_0}J_0(q_\perp\rho_0)\sin(\omega t)\delta_{m',m}\\&\quad\times\left[\left(m+\frac{1}{2}-\frac{1}{2}s\cos(\gamma)\right)\delta_{s',s}+\frac{1}{2}\sin(\gamma)\delta_{s',-s}\right].\end{aligned}\tag{23}$$

Importantly, in contrast to the RVB, spin flip can be triggered by AVB [recall that the eigenstates of $\hat{H}_0$ are not eigenstates of σ_z or $\hat{L}_z$; thus, for instance, $\partial_\varphi\Psi^s_m(\varphi)=i(m+1/2)\Psi^s_m(\varphi)-\frac{is}{2\sqrt{2\pi}}e^{i(m+1/2)\varphi}\nu^s(-\gamma,\varphi)$]. Further, the spin-flip transitions are proportional to the Rashba coefficient $\sin(\gamma)\propto\alpha_R$ (cf. Refs. [41,50] for EM homogeneous or OAM pulses).

For insight into how the azimuthally polarized beam affects the charge carriers, we study the extreme case of vanishing spin-orbit coupling, i.e., for $\gamma\to 0$. We start from an initial state characterized by equipopulated clockwise and counterclockwise angular momentum quantum numbers $m=-M,-M+1,\ldots,M-1,M$ (such as the ground state). For a 2D quantum ring without SOI, in the case of a small perturbation the time-dependent state wave functions read $\Psi_{nm}(\boldsymbol{r},t)=\Psi_{nm}(\boldsymbol{r})e^{-i\omega_{nm}t}+\delta\Psi_{nm}(\boldsymbol{r},t)$, where, according to Eq. (23),

$$\delta\Psi_{nm}(\boldsymbol{r},t)=+im\frac{\mu_B A_0}{\hbar}e^{im\varphi}\sum_{n'\neq n}\mathcal{R}^{\rm AVB}_{n'n}e^{-i\omega_{n'm}t}\mathcal{E}_{n'n}(t).\tag{24}$$

Here, $\mathcal{R}^{\rm AVB}_{n'n}=\int_0^\infty d\rho\,R_{n'm}(\rho)J_1(q_\perp\rho)R_{nm}(\rho)/\rho$ is the radial integral, while we assume a laser pulse of length T_p characterized by a temporal envelope function modeled as cosine squared, i.e., $\Omega(t)=\cos^2(\pi t/T_p)$ for $t\in[-T_p/2,T_p/2]$. Hence, the temporal function $\mathcal{E}_{n'n}(t)=\int_{-\infty}^t d\tau\,\sin(\omega\tau)\Omega(\tau)e^{i(\omega_{n'm}-\omega_{nm})\tau}$ dictates energy selection rules. Note that for a continuous wave (cw) we converge against Fermi's golden rule, i.e., $\mathcal{E}_{n'n}(t)\propto\delta(\omega_{n'm}-\omega_{nm}-\omega)$.

The corresponding induced (ring) current density reads

$$\begin{aligned}j_\varphi(\boldsymbol{r},t)&=j_{\rm charge}(\boldsymbol{r},t)+j_{\rm A}(\boldsymbol{r},t)\\&=\frac{e}{m_0}\sum_{n}^{\rm occ}\sum_{m=-M}^{M}\left\{\frac{\hbar}{r}{\rm Im}\{\Psi^*_{nm}(\boldsymbol{r},t)\partial_\varphi\Psi_{nm}(\boldsymbol{r},t)\}\right.\\&\quad\left.-e\boldsymbol{A}_{\rm AVB}(\boldsymbol{r},t)|\Psi_{nm}(\boldsymbol{r},t)|^2\right\}.\end{aligned}\tag{25}$$

Due to the conservation of the angular quantum number, the $\pm M$ state pair delivers the same (in magnitude and at any time t) but counterdirected current densities, and hence, $j_{\rm charge}(\boldsymbol{r},t)$ vanishes. The final (ring) current density is given by

$$\begin{aligned}j_\varphi(\boldsymbol{r},t)=j_{\rm A}(\boldsymbol{r},t)&=\frac{e^2A_0}{m_0}\left[\rho^0_e(r)+\delta\rho_e(r,t)\right]\\&\quad\times J_1(q_\perp\rho)\Omega(t)\sin(\omega t)\hat{e}_\varphi,\end{aligned}\tag{26}$$

where $\rho^0_e(r)=\sum_n\sum_{m=-M}^M|\Psi_{nm}(\boldsymbol{r},t)|^2$ is the initial (time-independent) charge density and the perturbative density is $\delta\rho_e(r,t)=\sum_n\sum_{m=-M}^M m^2(\mu_B^2A_0^2/\hbar^2)\left|\sum_{n'}\mathcal{R}^{\rm AVB}_{n'n}e^{-i\omega_{n'm}t}\mathcal{E}_{n'n}(t)\right|^2$. We have to remark that the mixing terms between $\Psi_{nm}(\boldsymbol{r},t)$ and $\delta\Psi_{nm}(\boldsymbol{r},t)$ vanish upon summation over the whole set of angular quantum numbers $m=-M,\ldots,M$. Thus, the (ring) current density in the φ direction is solely set by the vector-beam-driven charge density $\rho_e(r,t)=\rho^0_e(r)+\delta\rho_e(r,t)$ driven by the vector potential $\boldsymbol{A}_{\rm AVB}(\boldsymbol{r},t)$. It follows that the charge density oscillates with the frequency of the driving field, which means that, beyond transient effects, no directional time-averaged current is induced in the φ direction. Since the setup can be tuned to low frequencies, the effect should be observable. Note that for the AVB the coupling to the electric field component of the light-matter interaction vanishes since $\boldsymbol{r}\cdot\boldsymbol{E}_{\rm AVB}=0$ and no electrically induced transitions happen. In the (more general) 2D case radial currents are possible and depend on the strength of radial subband transitions $n\to n'$ characterized by $\mathcal{R}^{\rm AVB}_{n'n}$. Physically, they are due to inhomogeneities of the magnetic field (in the absence of the electric coupling) and are negligibly small in comparison to the subband transition driven by an RVB, i.e., smaller by a factor of $\mu_B/(ec\rho_0)$. Hence, a 1D ring where radial subbands are absent (and $\delta\Psi_{nm}$ vanish) is entirely sufficient for demonstrating the effects. Here, we find that for all times $\boldsymbol{\nabla}\cdot\boldsymbol{j}(\boldsymbol{r},t)\equiv 0$. It follows from the continuity equation that the incident light field does not change the electronic density, i.e., $\partial_t\rho_e(\boldsymbol{r},t)=0$. Therefore, our system remains locally and at all times neutral, and the resulting oscillating current is caused solely by the time-dependent magnetic vector potential $\boldsymbol{A}_{\rm AVB}(\boldsymbol{r},t)$ and falls thus in the class of a *dynamic Aharonov-Bohm effect*.

Experimentally, we may sense the action of the AVB by measuring the associated oscillating magnetic dipole moment

$$\begin{aligned}\boldsymbol{m}(t)&=\frac{1}{2}\int d\boldsymbol{r}\,\boldsymbol{r}\times\boldsymbol{j}(\boldsymbol{r},t)\\&=\frac{e^2A_0}{2m_0}\mathcal{M}(t)\sin(\omega t)\hat{e}_z,\end{aligned}\tag{27}$$

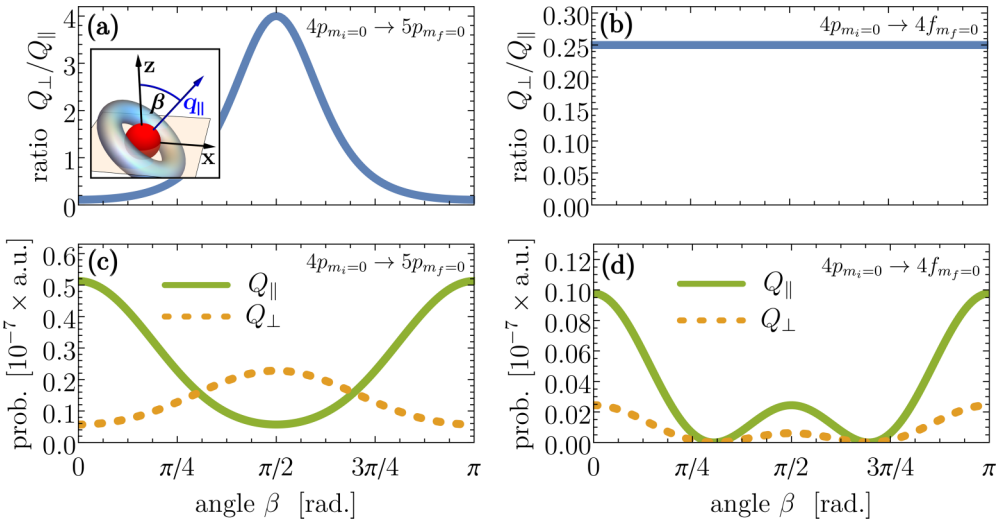

FIG. 3. Quadrupole transitions initiated by a vector laser pulse with a radial polarization. A comparison between the longitudinal and the transverse field contributions is shown. The inset in (a) illustrates the angle β between the optical axis of the incident vector beam (blue) and the quantization (z) axis of the atom (red sphere) as set by an external static magnetic field. Top row: The ratio between the quadrupole excitation probability, labeled by $Q_\perp$ and $Q_\parallel$, for the p-p and p-f transitions. Bottom row: Explicit quadrupole excitation probabilities for the p-p and p-f transitions. The field has a peak intensity of 3.51×10^{16} W/cm^2. The atom is on the optical axis and experiences a much lower intensity. The photon energy is tuned to $\hbar\omega = 4.37$ eV (for p-p transitions) or $\hbar\omega = 5.31$ eV (p-f transitions); all fields have a duration corresponding to 30 optical cycles. The static magnetic field is set to 10 T.

where $\mathcal{M}(t) = \int_0^\infty \rho d\rho\, \rho[\rho_e^0(r,t) + \delta\rho_e(r,t)]$. To confirm the insight obtained from first-order perturbation theory, we show the results of the numerical simulation of a quantum ring with same geometrical parameter as in the case for the RVB. Figure 2(b) shows the time-dependent magnetic moment in the z direction which is gathered from a full numerical quantum dynamic simulation. For the irradiated quantum ring we used the same parameters as for the RVB case. In line with the analytical predictions [Eq. (27)], the buildup and decay times are locked to the applied external field, pointing to a vanishing contribution $\pm j_{\text{charge}}(\boldsymbol{r}, t)$ to the whole current density [see Eq. (25)]. The transient $\boldsymbol{m}(t)$ vanishes once the pulse is off, but one may also induce an interference-driven quasistatic component by a combination of two AVBs with frequencies ω and 2ω (not shown here).

The spin-orbit coupling $\hat{H}_{\text{SOI}}(t)$ [see Eq. (11)] is mainly determined by the longitudinal component of the magnetic field of the AVB. The corresponding matrix elements take on the explicit form

$$M_{\text{SOI}}^{\text{AVB}}(t) = \left\langle \Psi_{m'}^{s'} \middle| \hat{H}_{\text{SOI}}^{\text{AVB}}(t) \middle| \Psi_m^s \right\rangle = \frac{e\alpha A_0}{\hbar} J_1(q_\perp \rho_0)[s\sin(\gamma)\delta_{s',s} + \cos(\gamma)\delta_{s',-s}] \times \sin(\omega t)\delta_{m',m}. \quad (28)$$

Thus, effectively, the AVB results in spin-flip transitions, even to first order in the light-matter interaction. The strength of these transitions is linear in SOI strength α_R. The matrix element indicates that even in the presence of SOI the AVB does not cause a change in the angular momentum state. This fact allows us to study pure spin dynamics while the orbital angular momentum is frozen. We conclude that a ubiquitous feature of the most common vector beam types (RVB and AVB) is that the orbital angular momentum of the electronic states is unaffected.

The further spin-dependent contribution to the AVB-matter interaction is given by $\hat{H}_z(t)$. It describes the direct interaction of the spin state with the magnetic field component of the vector beam. Generally, it is much weaker than the spin-orbit interaction, which follows from comparing the prefactors ($e\alpha/\hbar > \mu_B q$). Nonetheless, for completeness we provide an expression for the matrix elements of this light-matter interaction contribution. Notice that the magnetic field of the AVB also has a transverse component which couples to σ_r, leading again to spin-flip transitions. In addition to that, the strong longitudinal field [characterized by $J_0(q_\perp\rho)$] gives rise to a *dynamical* Zeeman effect. The matrix elements can be found analytically and read explicitly

$$M_z^{\text{AVB}}(t) = \left\langle \Psi_{m'}^{s'} \middle| H_z^{\text{AVB}} \middle| \Psi_m^s \right\rangle = \tfrac{1}{2} g_s \mu_B A_0 \{ q_\parallel J_1(q_\perp\rho_0)[s\sin(\gamma)\delta_{s',s} + \cos(\gamma)\delta_{s',-s}]\cos(\omega t) + q_\perp J_0(q_\perp\rho_0)[s\cos(\gamma)\delta_{s',s} - \sin(\gamma)\delta_{s',-s}]\sin(\omega t)\}\delta_{m',m}. \quad (29)$$

In practice, both spin-orbit coupling contributions bring about dynamical spin-flip processes, while the individual charge currents (associated with the orbital motion) sum to zero.

IV. ATOMS DRIVEN BY VECTOR BEAMS

Let us consider as a further case an atomic system in a strong magnetic field such that SOI is subsidiary to $\mu_B B_z(\hat{L}_z + g_s\hat{S}_z)$ (Paschen-Back effect). The electron states with the usual notation $|i\rangle = |n_i \ell_i m_i s_i\rangle$ are appropriate. Further, the atomic system is assumed to be located (trapped) on the optical axis of an incident vector beam, as already demonstrated experimentally for a $^{40}Ca^+$ ion by means of an OAM vortex

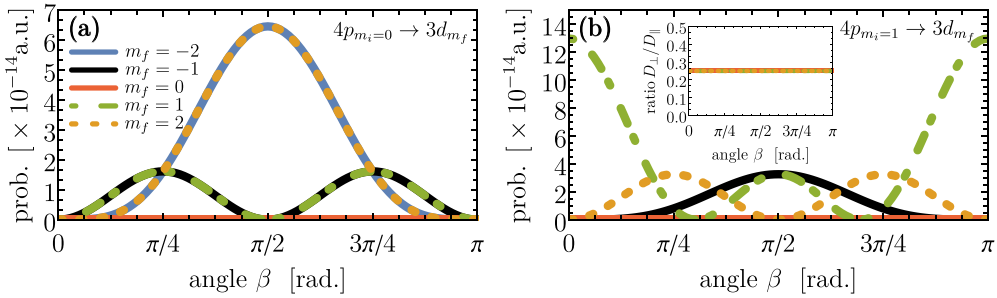

FIG. 4. Dipole transitions initiated by an azimuthally polarized vector laser pulse. The population of different magnetic sublevels dependent on the rotation angle β between the beam optical axis and the direction of an external static magnetic field. Two initial states, $4p_{m_i=0}$ and $4p_{m_i=1}$, are shown. Inset: The ratio between the dipole transition probabilities originating from the longitudinal and the transverse field contributions, labeled by $D_\perp$ and $D_\parallel$. Field parameters similar to those in Fig. 3 were used.

field [14]. The magnetic field sets the quantization axis (z axis), while the optical axis of the incident VB makes an angle $\beta = \measuredangle(\hat{e}_z, q_\parallel)$ with the z axis (shown in the inset in Fig. 3). We inspect Rydberg states $|i\rangle$ characterized by the principal, orbital, and magnetic quantum numbers n_i, ℓ_i, and m_i. For photoexcitation of higher Rydberg states the laser photon energy is such that the wave vector $q = \omega/c \ll 1$, and thus, we expand the oscillating functions in Eqs. (3) and (2) in a Taylor series up to terms of the first order: $J_1(x) = (1/2)x + O(x^3)$, $J_0 = 1 + O(x^2)$, and $\exp(ix) = 1 + ix + O(x^2)$. In the *local* frame $\{\rho', \varphi', z'\}$ rotated by β relative to the z axis, we employ the rotating-wave approximation and obtain for the first-order term of the field of the RVB:

$$\boldsymbol{A}_{\mathrm{RVB}}(\boldsymbol{r}', t) \approx -A_0 \left[\frac{1}{2} q_\perp \rho' \hat{e}_{\rho'} + i \frac{q_\perp}{q_\parallel} (1 + i q_\parallel z') \hat{e}_{z'} \right] e^{-i\omega t}. \tag{30}$$

Interestingly, the quadrupole terms, originating from the longitudinal and transverse field distributions, have the same prefactors.

Figure 3 shows the results for the photoexcitation process of a trapped Ca^+ ion starting from the initial $4p_{m_i=0}$ Rydberg state by a cw RVB. The nature of the matter interaction with a radially polarized vector beam is dominantly electric and is characterized by a strong dipole term stemming from the (electric) longitudinal component. However, one can discriminate between these dipolar and higher-order electron transitions by adjusting appropriately the photon energy to $\hbar\omega = \varepsilon_{5p} - \varepsilon_{4p}$ or $\hbar\omega = \varepsilon_{4f} - \varepsilon_{4p}$. The peak amplitude A_0 of the vector beam was chosen to yield a peak intensity of $3.51 \times 10^{16}\,\mathrm{W/cm^2}$. We have to remark that despite the large peak intensity the expected transition probabilities are rather small since the electric field amplitude modulates with ρ' near the optical axis where the ion is trapped (further, the prefactor for the transverse electric field is $A_0 \omega q_\perp$, and for the longitudinal field it is $A_0 \omega \tan\alpha$ with $\alpha = 1^\circ$). The left panels in Fig. 3 show the quadrupole transition probabilities $Q_\perp$ and $Q_\parallel$, resolved for the longitudinal and transverse field components, depending on the rotation angle β for the initial-final-state transition $4p_{m_i=0} \to 5p_{m_f=0}$. To be more precise, $Q_\perp$ refers to the quadrupole transition probability initiated by the transverse field component of the RVB vector potential, $A_\perp = -(1/2) A_0 q_\perp \rho' \hat{e}_{\rho'}$. Analogously, $Q_\parallel$ is the transition probability as a result of the action of the longitudinal field component $A_\parallel = -A_0 q_\perp z' \hat{e}_{z'}$. The variations in β of both quadrupole transition probabilities $Q_\parallel$ and $Q_\perp$ are evaluated numerically. We recall that β is an external parameter that can be varied experimentally, for instance, by changing the direction of the external static magnetic field. In this way $Q_\parallel$ and $Q_\perp$ can be discriminated, as evidenced by Fig. 3

Interestingly, for the orbital-momentum-conserving quadrupole transition with $\Delta\ell = \Delta m = 0$ the ratio $Q_\perp/Q_\parallel$ can be steered by rotating the incident vector field relative to the applied magnetic field (which sets the quantization axis). Parallel to the magnetic field, the ratio $Q_\perp/Q_\parallel = 1/9$ reveals the dominating longitudinal component, while at an angle of $\beta = 90^\circ$ (the RVB and magnetic field are perpendicularly polarized) the transverse component dominates the photoexcitation process since $Q_\perp/Q_\parallel = 4$. Therefore, in contrast to a conventional Gaussian mode we can find angular-momentum-conserving quadrupole transitions for all possible light field setups due to the special spatially inhomogeneous character of the vector beam.

The situation changes when exploring the $4p_{m_i=0} \to 4f_{m_f=0}$ quadrupole transition, which is characterized by $\Delta\ell = 2$. Here, it is not possible to change the ratio between the longitudinal and transverse field contributions since $Q_\perp/Q_\parallel = 1/4$ for all rotation angles β. Interestingly, we find rotating angles where the quadrupole transitions (from either the longitudinal or transverse field) vanish completely. For such a setup the whole photoexcitation probability of $4p_{m_i=0} \to 4f_{m_f=0}$ collapses.

For the azimuthal polarization the interaction is fully magnetic since $\boldsymbol{r} \cdot \hat{e}'_\varphi = 0$, and therefore, we have no coupling to the electron (note that $\boldsymbol{r} \cdot \hat{e}'_\varphi$ vanishes for every rotation angle β). With the same approximations as for the RVB the strong longitudinal field is given (up to first order in r) by $B_\parallel(\boldsymbol{r}', t) = i A_0 q_\perp (1 + i q_\parallel z') e^{-i\omega t} \hat{e}'_z$, while the transverse field $B_\perp(\boldsymbol{r}', t) = \frac{1}{2} A_0 q_\perp q_\parallel \rho' e^{-i\omega t} e'_\rho$. The homogeneous term in the longitudinal component provides no contribution to the photoinduced electron transition since it characterizes a monopole interaction. Consequently, as for the electric-type transitions in the case of the RVB, the effective contributions of the longitudinal and transverse field components are on equal footing, but the associated light-matter interaction is dipolar.

In Fig. 4 we show the dipole transitions initiated by the spatially inhomogeneous magnetic field of the AVB for two different initial states, $4p_{m_i=0}$ and $4p_{m_f=1}$. As expected, for

$\beta = 0^\circ$ no photoexcitation processes can be observed since the magnetic field does not act on the electron states with zero angular velocity ($m_i = 0$). However, as inferred from Fig. 4(a), for finite rotating angles one can populate final magnetic substates with $m_f \neq 0$. Prominent setups are given by $\beta = \pm 45^\circ$, where states with $m_f = \pm 1$ and $m_f = \pm 2$ are equally excited, while for $\beta = \pm 90^\circ$ the final states are fully characterized by $m_f = \pm 2$. Note that due to the presence of the external magnetic field, which sets the quantization axis and shifts the energy of the individual magnetic substates (Zeeman effect), the photon energy of the incident AVB has to be adjusted to the specific transitions, i.e., $\hbar\omega = \varepsilon_{n_f \ell_f m_f} - \varepsilon_{n_i \ell_i m_i}$.

In Fig. 4(b) the dipolar photoexcitation transitions are depicted for the initial state $4p_{m_i=1}$. As expected for $\beta = 0^\circ$, the only state which can be excited is characterized by $m_f = 1$ since in this case the interaction between the electron and the light field is angular momentum conserving, i.e., $\Delta m = 0$. Interestingly, at $\beta = \pm 90^\circ$ the photoexcitation probability of $m_f = \pm 1$ is the same, while at $\beta = \pm 45^\circ$ the dominating final state is characterized by the magnetic quantum number $m_f = 2$. Another striking feature, in contrast to the RVB, is the ratio between transverse and longitudinal field contributions, which is always given by $D_\perp / D_\parallel = 0.25$ and thus cannot be manipulated by the rotation angle β.

V. SUMMARY AND OUTLOOK

We explored the nature of the interaction of atomic and low-dimensional quantum systems (rings) with EM fields with spatially inhomogeneous polarization states, called vector beams. In particular, we focused on cylindrical beams with radial or azimuthal polarization. Although these beams share some common features with vortex beams carrying orbital angular momentum, like the intensity profile, their effect on charge carriers is fundamentally different. For the investigated systems, radially polarized vector beams trigger, via electric transitions, radial charge oscillations. Azimuthally polarized vector beams generate, via a magnetic interaction, oscillating magnetic moments. Despite the presence of the electric field in the AVB, it subsumes in a way that it does not affect the charge. The interaction with the AVB is solely due to the magnetic vector potential and can thus be interpreted as a *dynamic* Aharonov-Bohm effect. In contrast to OAM-carrying fields, no unidirectional, time-averaged currents are generated by AVB or by RVB. Atomic targets subject to radially polarized light fields show angular-momentum-conserving quadrupole transitions which can be manipulated in magnitude by rotating the field relative to the quantization axis set by an external static magnetic field. When photoexciting with an azimuthally polarized field, the special field structure makes it possible to select different magnetic sublevels (in the final state) by rotating the laser field relative to the quantization axis of the atomic target.

ACKNOWLEDGMENT

This work was partially supported by the DFG through Grants No. SPP1840 and No. SFB TRR 227.

APPENDIX A

The electric field of a radially polarized vector beam (RVB) is given by

$$E_r^{\mathrm{RVB}}(\boldsymbol{r}, t) = A_0 \omega_x J_1(q_\perp \rho) \sin(q_\parallel z - \omega_x t), \tag{A1a}$$

$$E_\varphi^{\mathrm{RVB}}(\boldsymbol{r}, t) = 0, \tag{A1b}$$

$$E_z^{\mathrm{RVB}}(\boldsymbol{r}, t) = A_0 \omega_x \frac{q_\perp}{q_\parallel} J_0(q_\perp \rho) \cos(q_\parallel z - \omega_x t), \tag{A1c}$$

while the associated magnetic field reads

$$B_r^{\mathrm{RVB}}(\boldsymbol{r}, t) = 0, \tag{A2a}$$

$$B_\varphi^{\mathrm{RVB}}(\boldsymbol{r}, t) = A_0 \frac{q_\perp^2 + q_\parallel^2}{q_\parallel} J_1(q_\perp \rho) \sin(q_\parallel z - \omega_x t), \tag{A2b}$$

$$B_z^{\mathrm{RVB}}(\boldsymbol{r}, t) = 0. \tag{A2c}$$

In the same vein, the electromagnetic fields of the azimuthally polarized vector beam (AVB) as the sum of two antiparallel Bessel beams read

$$E_r^{\mathrm{AVB}}(\boldsymbol{r}, t) = 0, \tag{A3a}$$

$$E_\varphi^{\mathrm{AVB}}(\boldsymbol{r}, t) = -A_0 \omega_x J_1(q_\perp \rho) \cos(q_\parallel z - \omega_x t), \tag{A3b}$$

$$E_z^{\mathrm{AVB}}(\boldsymbol{r}, t) = 0, \tag{A3c}$$

and

$$B_r^{\mathrm{AVB}}(\boldsymbol{r}, t) = A_0 q_\parallel J_1(q_\perp \rho) \cos(q_\parallel z - \omega_x t), \tag{A4a}$$

$$B_\varphi^{\mathrm{RVB}}(\boldsymbol{r}, t) = 0, \tag{A4b}$$

$$B_z^{\mathrm{AVB}}(\boldsymbol{r}, t) = -A_0 q_\perp J_0(q_\perp \rho) \sin(q_\parallel z - \omega_x t). \tag{A4c}$$

APPENDIX B

Using the vector potential in the Poincaré gauge, i.e., $\boldsymbol{A}'(\boldsymbol{r}, t) = -\boldsymbol{r} \times \int_0^1 d\lambda\, \lambda \boldsymbol{B}(\lambda \boldsymbol{r}, t)$, where the vector field satisfies $\boldsymbol{r} \cdot \boldsymbol{A}'(\boldsymbol{r}, t) \equiv 0$, we derive the expression for the magnetic contribution to the interaction Hamiltonian $\hat{H}_{\mathrm{int}}(t)$ from the minimal coupling scheme:

$$H_{\mathrm{magn}}(t) = -\frac{e}{2m_0}[\boldsymbol{p} \cdot \boldsymbol{A}'(\boldsymbol{r}, t) + \boldsymbol{A}'(\boldsymbol{r}, t) \cdot \boldsymbol{p}]. \tag{B1}$$

Inserting $\boldsymbol{A}'(\boldsymbol{r}, t)$ and applying the fundamental identities $\boldsymbol{p} \cdot (\boldsymbol{r} \times \boldsymbol{B}) = (\boldsymbol{p} \times \boldsymbol{r}) \cdot \boldsymbol{B}$ and $(\boldsymbol{r} \times \boldsymbol{B}) \cdot \boldsymbol{p} = \boldsymbol{B} \cdot (\boldsymbol{p} \times \boldsymbol{r})$, we find

$$H_{\mathrm{magn}}(t) = \frac{e}{2m_0}(\boldsymbol{p} \times \boldsymbol{r}) \cdot \int_0^1 d\lambda\, \lambda \boldsymbol{B}(\lambda \boldsymbol{r}, t) + \frac{e}{2m_0} \int_0^1 d\lambda\, \lambda \boldsymbol{B}(\lambda \boldsymbol{r}, t) \cdot (\boldsymbol{p} \times \boldsymbol{r}). \tag{B2}$$

From elementary quantum-mechanical algebra we know that

$$(\boldsymbol{p} \times \boldsymbol{r}) \cdot \boldsymbol{B} = \boldsymbol{B} \cdot (\boldsymbol{p} \times \boldsymbol{r}) - [\boldsymbol{B}, (\boldsymbol{p} \times \boldsymbol{r})]_-. \tag{B3}$$

Using $\boldsymbol{p}\times\boldsymbol{r}=-\boldsymbol{r}\times\boldsymbol{p}$, we can find the commutator

$$\begin{aligned}[\boldsymbol{B},(\boldsymbol{p}\times\boldsymbol{r})]_- &= [(\boldsymbol{r}\times\boldsymbol{p}),\boldsymbol{B}]_- \\ &= \varepsilon_{ijk}[x_j p_k, B_i]_- \\ &= \varepsilon_{ijk}x_j[p_k,B_i]_- + \varepsilon_{ijk}\underbrace{[x_j,B_i]_-}_{=0}p_k \\ &= \boldsymbol{r}\cdot(\boldsymbol{p}\times\boldsymbol{B}).\end{aligned} \tag{B4}$$

By now using the Ampère-Maxwell law [54] the commutator can be reformulated further:

$$\begin{aligned}[\boldsymbol{B},(\boldsymbol{p}\times\boldsymbol{r})]_- &= \boldsymbol{r}\cdot(\boldsymbol{p}\times\boldsymbol{B}) \\ &= -i\hbar\boldsymbol{r}\cdot[\boldsymbol{\nabla}\times\boldsymbol{B}(\boldsymbol{r},t)] \\ &= -\frac{i\hbar}{c^2}\boldsymbol{r}\cdot\frac{\partial\boldsymbol{E}(\boldsymbol{r},t)}{\partial t}.\end{aligned} \tag{B5}$$

Furthermore, by assuming a harmonic wave we find that $\partial_t\boldsymbol{E}(\boldsymbol{r},t)\sim-\omega_x\boldsymbol{E}(\boldsymbol{r},t)$ and obtain the final expression for the Hamiltonian containing the commutator:

$$\begin{aligned}H_{\text{magn}}^{\text{comm.}} &= -\int_0^1 d\lambda\,\lambda\frac{e}{2m}[\boldsymbol{B},(\boldsymbol{p}\times\boldsymbol{r})]_- \\ &= \frac{ie}{2}\frac{\hbar\omega_x}{m_0c^2}\int_0^1 d\lambda\,\lambda\boldsymbol{r}\cdot\boldsymbol{E}(\boldsymbol{r},t),\end{aligned} \tag{B6}$$

which can be safely neglected by noticing that the prefactor $\hbar\omega_x/m_0c^2<10^{-4}$ even for photon energies in the (X)UV regime. Furthermore, in the case of an AVB $\boldsymbol{r}\cdot\boldsymbol{E}(\boldsymbol{r},t)\equiv0$ (azimuthal polarization). As a consequence, the magnetic part of the interaction Hamiltonian is

$$\begin{aligned}H_{\text{magn}}(t) &= \frac{e}{m_0}\left[-\int_0^1 d\lambda\,\lambda\boldsymbol{B}(\lambda\boldsymbol{r},t)\right]\cdot(\boldsymbol{r}\times\hat{\boldsymbol{p}}) \\ &= 2\boldsymbol{B}'(\boldsymbol{r},t)\cdot\widehat{\boldsymbol{m}}_B,\end{aligned} \tag{B7}$$

where $\boldsymbol{B}'(\boldsymbol{r},t)=-\int_0^1 d\lambda\,\lambda\boldsymbol{B}(\lambda\boldsymbol{r},t)$ and the magnetic moment operator is $\widehat{\boldsymbol{m}}_B=(e/2m)\boldsymbol{r}\times\hat{\boldsymbol{p}}$.

[1] T. Brabec and F. Krausz, Rev. Mod. Phys. **72**, 545 (2000).
[2] H. Petek and S. Ogawa, Prog. Surf. Sci. **56**, 239 (1997).
[3] J. Ng, Z. Lin, and C.T. Chan, Phys. Rev. Lett. **104**, 103601 (2010).
[4] X. Hao, C. Kuang, T. Wang, and X. Liu, Opt. Lett. **35**, 3928 (2010).
[5] R. Dorn, S. Quabis, and G. Leuchs, Phys. Rev. Lett. **91**, 233901 (2003).
[6] M. Kang, J. Chen, X.-L. Wang, and H.-T. Wang, J. Opt. Soc. Am. B **29**, 572 (2012).
[7] T. Bauer, S. Orlov, U. Peschel, P. Banzer, and G. Leuchs, Nat. Photonics **8**, 23 (2014).
[8] V. Parigi, V. D'Ambrosio, C. Arnold, L. Marrucci, F. Sciarrino, and J. Laurat, Nat. Commun. **6**, 7706 (2015).
[9] V. D'Ambrosio, E. Nagali, S. P. Walborn, L. Aolita, S. Slussarenko, L. Marrucci, and F. Sciarrino, Nat. Commun. **3**, 961 (2012).
[10] G. Vallone, V. D'Ambrosio, A. Sponselli, S. Slussarenko, L. Marrucci, F. Sciarrino, and P. Villoresi, Phys. Rev. Lett. **113**, 060503 (2014).
[11] C. Gabriel, A. Aiello, W. Zhong, T. G. Euser, N. Y. Joly, P. Banzer, M. Förtsch, D. Elser, U. L. Andersen, C. Marquardt, P. S. J. Russell, and G. Leuchs, Phys. Rev. Lett. **106**, 060502 (2011).
[12] C. Guclu, M. Veysi, and F. Capolino, ACS Photonics **3**, 2049 (2016).
[13] K. Y. Bliokh, F. Rodríguez-Fortuño, F. Nori, and A. V. Zayats, Nat. Photonics **9**, 796 (2015).
[14] C. T. Schmiegelow, J. Schulz, H. Kaufmann, T. Ruster, U. G. Poschinger, and F. Schmidt-Kaler, Nat. Commun. **7**, 12998 (2016).
[15] J. Wätzel and J. Berakdar, Sci. Rep. **6**, 21475 (2016).
[16] J. Wätzel, Y. Pavlyukh, A. Schäffer, and J. Berakdar, Carbon **99**, 439 (2016).
[17] J. R. Zurita-Sánchez and L. Novotny, J. Opt. Soc. Am. B **19**, 2722 (2002).
[18] B. Hanewinkel, A. Knorr, P. Thomas, and S.W. Koch, Phys. Rev. B **55**, 13715 (1997).
[19] M. Veysi, C. Guclu, and F. Capolino, J. Opt. Soc. Am. B **32**, 345 (2015).
[20] R. Oron, S. Blit, N. Davidson, A. A. Friesemzeev Bomzon, E. Hasman, A. A. Friesem, and Z. Bomzon, Appl. Phys. Lett. **77**, 3322 (2000).
[21] S. C. Tidwell, D. H. Ford, and W. D. Kimura, Appl. Opt. **29**, 2234 (1990).
[22] E. G. Churin, J. Hobfeld, and T. Tschudi, Opt. Commun. **99**, 13 (1993).
[23] M. Stalder and M. Schadt, Opt. Lett. **21**, 1948 (1996).
[24] S. Tripathi and K. C. Toussaint, Opt. Express **20**, 10788 (2012).
[25] G. Milione, H. I. Sztul, D. A. Nolan, J. Kim, M. Etienne, J. McCarthy, J. Wang, and R. R. Alfano, in *CLEO Science and Innovations* (Optical Society of America, Washington, D.C., 2011), p. CTuB2.
[26] B. Memarzadeh and H. Mosallaei, Opt. Lett. **36**, 2569 (2011).
[27] N. Yu, P. Genevet, M. A. Kats, F. Aieta, J.-P. Tetienne, F. Capasso, and Z. Gaburro, Science **334**, 333 (2011).
[28] N. Yu, F. Aieta, P. Genevet, M. A. Kats, Z. Gaburro, and F. Capasso, Nano Lett. **12**, 6328 (2012).
[29] Z. Bomzon, G. Biener, V. Kleiner, and E. Hasman, Opt. Lett. **27**, 285 (2002).
[30] M. Beresna, M. Gecevičius, P. G. Kazansky, and T. Gertus, Appl. Phys. Lett. **98**, 201101 (2011).
[31] X. Yi, X. Ling, Z. Zhang, Y. Li, X. Zhou, Y. Liu, S. Chen, H. Luo, and S. Wen, Opt. Express **22**, 17207 (2014).
[32] Y. Liu, X. Ling, X. Yi, X. Zhou, H. Luo, and S. Wen, Appl. Phys. Lett. **104**, 191110 (2014).
[33] Y. Saito, M. Kobayashi, D. Hiraga, K. Fujita, S. Kawano, N. I. Smith, Y. Inouye, and S. Kawata, J. Raman Spectrosc. **39**, 1643 (2008).
[34] H. Wang, L. Shi, B. Lukyanchuk, C. Sheppard, and C. T. Chong, Nat. Photonics **2**, 501 (2008).

[35] M. Meier, V. Romano, and T. Feurer, Appl. Phys. A **86**, 329 (2007).
[36] Q. Zhan, Opt. Express **12**, 3377 (2004).
[37] B. Sbierski, G. F. Quinteiro, P. I. Tamborenea, Q. Zhan, C. Gabriel, A. Aiello, W. Zhong, T. G. Euser, N. Y. Joly, P. Banzer, M. Förtsch, D. Elser, U. L. Andersen, C. Marquardt *et al.*, J. Phys. Condens. Matter **25**, 385301 (2013).
[38] G. F. Quinteiro and T. Kuhn, Phys. Rev. B **90**, 115401 (2014).
[39] L. Allen, M. W. Beijersbergen, R. J. C. Spreeuw, and J. P. Woerdman, Phys. Rev. A **45**, 8185 (1992).
[40] A. M. Yao and M. J. Padgett, Adv. Opt. Photonics **3**, 161 (2011).
[41] G. F. Quinteiro, P. I. Tamborenea, and J. Berakdar, Opt. Express **19**, 26733 (2011).
[42] V. Garces-Chavez, J. Arlt, K. Dholakia, K. Volke-Sepulveda, and S. Chavez-Cerda, J. Opt. B **4**, 82 (2002).
[43] C. Cohen-Tannoudji, J. Dupont-Roc, and G. Grynberg, *Photons and Atoms: Introduction to Quantum Electrodynamics* (Wiley-Interscience, New York, 1989).
[44] C. Cohen-Tannoudji, J. Dupont-Roc, G. Grynberg, and P. Thickstun, *Atom-Photon Interactions: Basic Processes and Applications*, Wiley Online Library (Wiley, New York, 1992).
[45] G. F. Quinteiro, D. E. Reiter, and T. Kuhn, Phys. Rev. A **95**, 012106 (2017).
[46] D. Frustaglia and K. Richter, Phys. Rev. B **69**, 235310 (2004).
[47] B. Molnár, P. Vasilopoulos, and F. M. Peeters, Phys. Rev. B **72**, 075330 (2005).
[48] J. S. Sheng and K. Chang, Phys. Rev. B. **74**, 235315 (2006).
[49] P. Földi, O. Kálmán, M. G. Benedict, and F. M. Peeters, Phys. Rev. B **73**, 155325 (2006).
[50] Z. G. Zhu and J. Berakdar, Phys. Rev. B. **77**, 235438 (2008).
[51] M. Iyoda, J. Yamakawa, and M. J. Rahman, Angew. Chem., Int. Ed. Engl. **50**, 10522 (2011).
[52] K. Choi and A. D. Hamilton, Coord. Chem. Rev. **240**, 101 (2003).
[53] J. F. Stoddart, Angew. Chem., Int. Ed. Engl. **56**, 11094 (2017).
[54] J. D. Jackson, *Classical Electrodynamics*, Wiley Online Library (Wiley, New York, 1975).